Fabrication of highly porous ZnO/Ag$_2$O nanoparticles embedded in N-doped graphitic carbon for photocatalytic degradation of tetracycline

Norah Alhokbany, Tansir Ahamad [*], Saad M. Alshehri

Department of Chemistry, King Saud University, Riyadh 11451, Saudi Arabia

ABSTRACT

In the present study, we have successfully fabricated ZnO/Ag$_2$O nanoparticles embedded in nitrogen doped carbon based nanocomposites (ZnO/Ag$_2$O-NDC). The fabricated nanocomposites were characterized by several analytical techniques. The photocatalytic performance was inspected by the degradation of tetracycline (TC) under visible light. The fabricated nanocomposites show excellent photocatalytic degradation performance, which can degrade approximately 90.7% of TC within 60 min at nearly neutral pH 7, and the degradation rate constant was found to be 0.0083 min^{-1}. Moreover, the optimal composite exhibited excellent stability, indicating its suitability for reuse. Reasonable pathways of antibiotic degradation were proposed based on the detected intermediates during the degradation, where the $^{\bullet}$OH and $O_2^{\bullet -}$ played a dominant role. It was also noticed that the N-doped graphitic carbon acts as the framework and promotes the electron transfer, and the ZnO acts as an effective photocatalyst while Ag$_2$O as an electron trapping agent to enhance the visible light activity.

1. Introduction

Nowadays, several undesired products such as dyes, heavy metals, chlorinated compounds, pesticides and pharmaceuticals are exposed to the environment and cause a serious challenge globally. Among these pollutants, antibiotics are one of the persistent pollutants and exist in the natural environment [1–4]. Tetracycline (TC) is one of the most famous antibiotics, used to treat a wide range of bacteria for humans and animals. However, after administration of tetracycline to humans, and animals cannot completely metabolize, resulting in a large amount of TC was exposed to the environment which lead to serious effects to the ecosystem and public health [5–7]. Therefore, the effective treatment of these antibiotics into wastewater systems becomes a major challenge. Currently, several techniques have been used to treat TC and other organic pollutants into wastewater including ion exchange, coagulation, filtration with coagulation, precipitation, ozonation, adsorption, reverse osmosis, advanced oxidation processes and photocatalytic degradation [8–10]. Among these techniques, photocatalytic degradation has much attention due to its outstanding advantage (economic, efficient, and green feature) [11–14]. To date several semiconductors based photocatalyst such as TiO$_2$, ZnS, CuO/CuO$_2$, CoFe$_3$O$_4$, NiFe$_3$O$_4$, MoS$_2$, Ag$_3$PO$_4$ and g-C$_3$N$_4$ have been used for the photocatalytic degradation of TC. However, each semiconductor has their own advantage/ disadvantage

and limitations [15–18]. Among these semiconductors, ZnO based photocatalyst are one of the most promising agents because of their extraordinary properties such as excellent chemical stability, low cost, and eco-friendly compound [19–21]. However, the large bandgap (3.37 eV), photo-corrosion and the rapid recombination of charge carriers, low response to visible light of ZnO restrict its photocatalytic applications. Therefore, it is essential to modify ZnO for the enhancement of its physicochemical and optical properties, especially rapid recombination of charge carriers [22–24]. The physicochemical and optical properties of the ZnO can be tuned using several supporting materials such as graphite carbon, CNTs, graphene, g-C$_3$N$_4$, other metal oxide [25–27]. The utilization of graphite carbon enhances the chemical stability, sorption activity, and corrosion resistance of the photocatalyst. On the other hand, the coupling with narrow band semiconductors such as SnO$_2$, Bi$_2$O$_3$, Cu$_2$O, MoS$_2$ and Ag$_2$O can improve the absorption to visible-light region and control the photogenerated charge recombination [28–30]. Among these narrow band gap semiconductors, Ag$_2$O is a p-type semiconductor with a narrow band gap energy varying from 1.2 to 1.5 eV is favorable to prepare composite with ZnO [31–33]. The photogenerated charge carriers can be effectively separated due the electron trapping behavior of Ag$_2$O, which can reduce the probability of recombination of electrons and holes, resulting in greatly enhanced optical properties [34–36]. In the present study, a hetrostructure

ZnO/Ag$_2$O was fabricated in N-doped carbon using hydrothermal and post calcination. The physicochemical and optical properties of the ZnO/Ag$_2$O-NDC nanocomposites were tuned with various ratios of Ag$_2$O to ZnO and used for the photocatalytic degradation of TC under visible light. The effect of pH, initial concentration and effect of scavengers and the kinetics was also studied to know the mechanism of photocatalytic degradation for TC. The formation of the photogenerated spices and intermediates during the photocatalytic degradation were determined using ESR and GC-Mass respectively.

2. Experiment

2.1. Materials

Zinc nitrate Zn(NO$_3$)$_2$.6H$_2$O, silver nitrate AgNO$_3$, egg albumen, hydrogen peroxide and tetracycline were purchased from Sigma Aldrich (Munich, Germany) and directly used without further purification. Milli-Q water was used throughout all experiments.

2.2. Fabrication of the nanocomposites (ZnO/Ag$_2$O-NDC)

The nanocomposite was fabricated using a single source precursor and fresh egg albumen was used as a source of N and carbon. Firstly, the metallic and bimetallic polymer-metal complex was prepared by mixing egg albumen with zinc nitrate and silver nitrate details are provided in supporting information. To fabricate the ZnO-NDC, Ag$_2$O-NDC, ZnO/Ag$_2$O(10%)-NDC, ZnO/Ag$_2$O(10%)-NDC, ZnO/Ag$_2$O(15%)-NDC and ZnO/Ag$_2$O(20%)-NDC nanocomposites the corresponding polymer-metal complex was transferred into an autoclave and heated at 200 °C for 24 h. The resulting hydrochar was filtered, washed and dried under vacuum. The fabricated hydrochar was further heat treated at 800 °C under the flow of argon with 5 °C/ min heating rate to get the nanocomposite. The resulting nanocomposite was washed several times using distilled water and dried in vacuum. The fabricated nanocomposites were characterized using several analytical techniques such as FTIR, TGA, XRD, Raman, BET (N$_2$ adsorption desorption), SEM, TEM/HRTEM, DSR spectra and XPS, their details are provided in supplementary information. The fabricated nanocomposites were used for the photocatalytic degradation of TC and the details of experiments are also given in supporting information.

3. Results and discussion

3.1. Characterization of ZnO/Ag$_2$O-NDC nanocomposites

The ZnO/Ag$_2$O-NDC based photocatalyst were fabricated using polymer bimetallic complexes, which were fabricated with egg albumin, zinc nitrate and silver nitrate as summarized in Fig. 1. The FTIR spectra of the ZnO/Ag$_2$O(15%)-NDC, ZnO-NDC and Ag$_2$O-NDC shown in Fig. 2 (a), while the FTIR spectra of other nanocomposites were illustrated in supporting figure SF1(a). The results support successfully fabrication of N-doped carbon. The presence of several functional groups including O-H, N-H, =C-H, -CH$_2$, C≡N, C≡C, C-N and O-C were supported with their corresponding peaks, which appear at 3421, 3240, 3042, 2960–2845, 1652, 1548, 1412 and 1132 cm^{-1} respectively.

Moreover, the peaks at 479 and 530 cm^{-1} support the presence of ZnO and Ag$_2$O nanoparticles in the NDC matrix [37–39]. It was noticed that in the case of ZnO/Ag$_2$O-NDC another peak at 530 cm^{-1} was noticed that support the presence of Ag$_2$O nanoparticles.

These results support the successful fabrication of the ZnO/Ag$_2$O-NDC nanocomposite. The XRD patterns of the fabricated nanocomposites are illustrated in Fig. 2(b), the XRD spectra of the ZnO-NDC show the diffraction peaks at 2θ = 31.80°, 34.39°, 36.14°, 47.43°, 56.49°, 62.63°, 66.28° and 67.71° assigned to 100, 002, 101, 102, 110, 103, 200 and 112, respectively support the formation of hexagonal wurtzite ZnO (JCPDs Card No. 36–1451) [40–42]. While the XRD spectra of Ag$_2$O-NDC show the peaks at 2θ of 32.98°, 38.13°, 55.81° and 64.43° are attributed to the 111, 200, 220 and 311 diffraction planes of cubic phase of Ag$_2$O respectively (JCPDs Card No. 41–1104) [43,44]. The XRD spectra of the ZnO/Ag$_2$O-NDC nanocomposites show mixed peaks for both the ZnO and Ag$_2$O and the intensity of the peaks belongs to Ag$_2$O increases with the increase the amount of Ag$_2$O that support the co-existence of two phases in the nanocomposites. Additionally, the broad peak at 25.52° assigned to (002) plane of graphite carbon which was observed in all the nanocomposites. No peak related to any impurity or unreacted metal was observed which confirmed that the nanocomposites mainly contain ZnO and Ag$_2$O nanoparticles.

The porosity and surface area of as fabricated nanocomposites were determine using nitrogen adsorption/desorption isothermal measurement and exhibited the type IV isotherm with a distinct hysteresis loop which indicates that a large number of meso-pore are present in the nanocomposites as shown in Fig. 3(a) and supporting figure SF-1(b). The BET specific surface area of ZnO-NDC, Ag$_2$O-NDC, ZnO/Ag$_2$O-NDC (5%) and ZnO/Ag$_2$O-NDC (15%) was found to be 482.2 m^2 g^{-1}, 437.6 m^2 g^{-1},
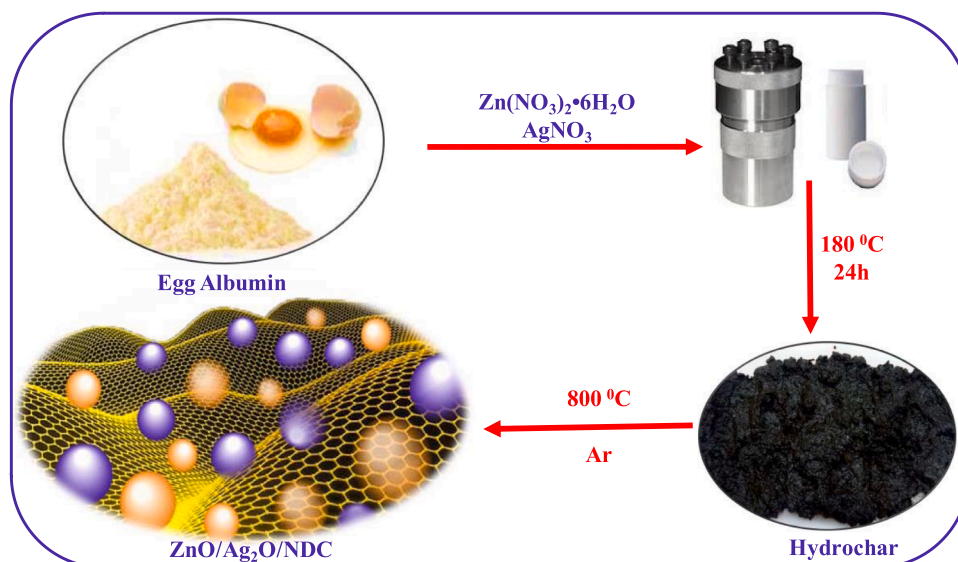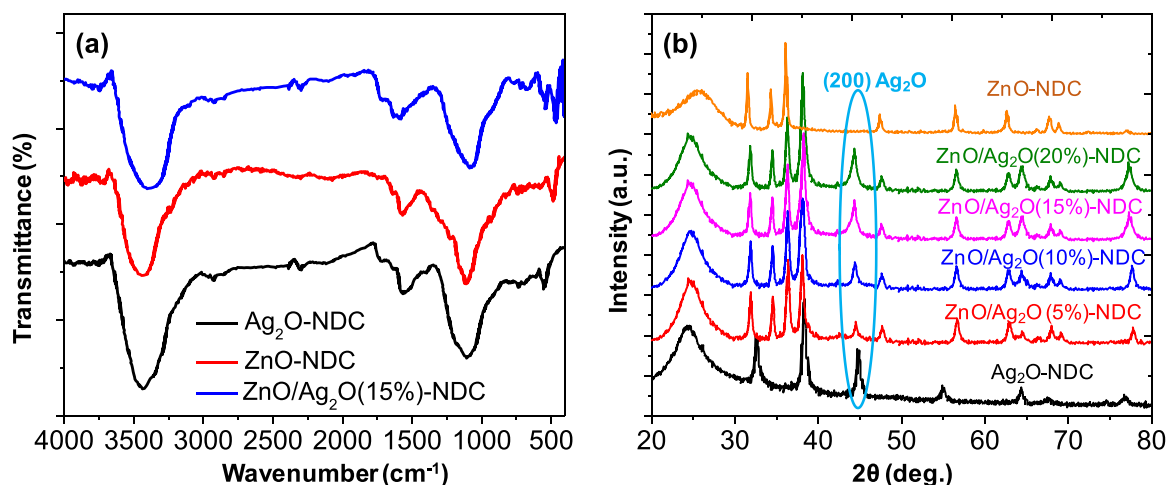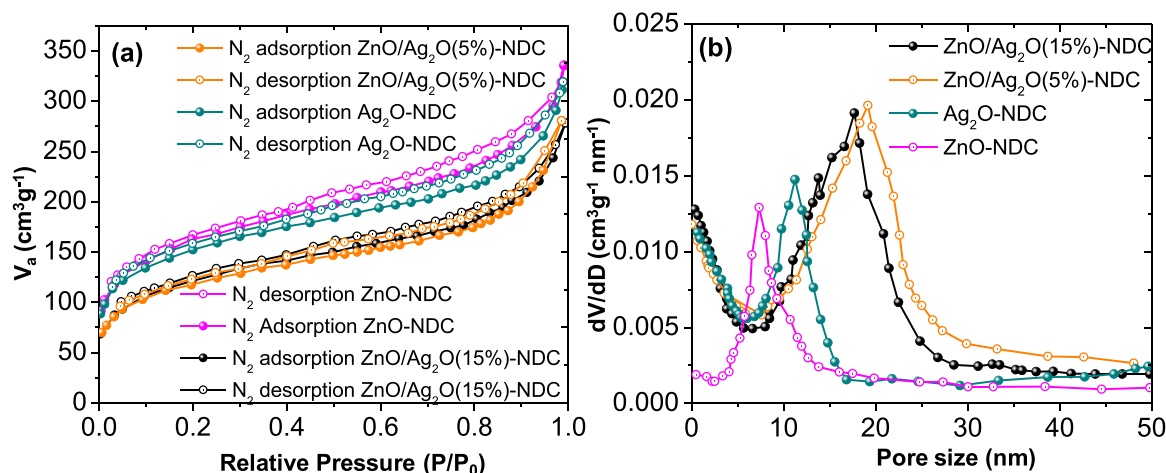

Fig. 1. The synthesis routes for ZnO/Ag$_2$O-NDC nanocomposite.

Fig. 2. (a) FTIR spectra and (b) XRD spectra curves of ZnO-NDC, Ag$_2$O-NDC, ZnO/Ag$_2$O(5%)-NDC, ZnOAg$_2$O(10%)-NDC, ZnO/Ag$_2$O(15%)-NDC, and ZnO/Ag$_2$O (20%)-NDC nanocomposites.

Fig. 3. (a) N$_2$ adsorption and desorption isotherm (b) pores size distribution of ZnO-NDC, Ag$_2$O-NDC, ZnO/Ag$_2$O(5%)-NDC,and ZnO/Ag$_2$O(15%)-NDC nanocomposites.

442.8 m^2 g^{-1}and 456.3 m^2 g^{-1} respectively. As shown in Fig. 3(b), the narrow size pore distribution was found in the range of 6–9 nm and the average pore volumes of the nanocomposites were found in the range of 0.28–42 cm^3 g^{-1}. The large specific surface area of the nanocomposites is considerably favorable for the adsorption of TC and provide more active sites for photocatalytic degradation.

The XPS is used to inspect the chemical composition and the surface chemical states of the elements present in the nanocomposite. The XPS spectra of Ag$_2$O-NDC, ZnO-NDC and ZnO/Ag$_2$O(15%)-NDC are illustrated in Fig. 4(a). The XPS spectrum of ZnO/Ag$_2$O(15%)-NDC shows the presence of C, N, Zn, Ag and O elements. As shown in Fig. 4(b), the C1s spectrum was deconvoluted into four peaks at 284.54 eV, 285.44 eV, 286.13 eV and 287.14 eV corresponding to the C-C, C=C, C-V/C≡N and C-O groups [45]. The N 1 s peaks was split in to three peaks and observed 398.91 eV, 399.79 eV, and 401.83 eV assigned to the pyridine-N, pyrrolic-N, and graphitic-N, respectively and illustrated in Fig. 4(c) [46]. The XPS spectrum of Zn 2p as shown in Fig. 4(d) showed two main peaks with binding energies at 1043.63 eV and 1020.62 eV characteristic doublets of Zn 2p$_{1/2}$ and Zn 2p$_{3/2}$, which were essentially identical binding energies for the Zn 2p orbital with spin orbital splitting about to 23.0 eV in accord with Zn(II). The Ag 2p XPS spectrum as shown in Fig. 4(e), deconvoluted into two peaks at 368.29 and 374.28 eV corresponding to Ag 3d$_{5/2}$ and Ag 3d$_{3/2}$, which supporting

the presence of Ag$^+$ as Ag$_2$O, which is agree with the XRD results [47, 48]. However slightly change in the pack position of Zn 2p was noticed in the case after formation of hetrostructure when compared with ZnO-NDC. As shown in Fig. 4(f), O 1 s spectrum can be divided into three peaks and observed at 529.56, 530.85 and 531.62 eV and assigned to the Ag-O, C-O/O-H, and Zn-O function groups [49,50]. The morphology of the nanocomposite was measured by SEM and TEM. As shown in Fig. 5 (a), the SEM image of ZnO/Ag$_2$O(15%)-NDC shows the highly porous surface and ZnO and Ag$_2$O nanoparticles were embedded into the carbon matrix. The ZnO nanoparticles were found spherical in shape and with a ranging from 20 nm to 30 nm. On the other hand, the Ag$_2$O particle sizes were in the range of 13–18 nm. For further details of the morphology, TEM examinations have been carried out as shown in Fig. 5 (b). The average diameter of the ZnO and Ag$_2$O nanoparticles were found to be about 20–30 nm and 12–20 nm, respectively and were uniformly embedded into graphite carbon matrix which is consistent with the results of SEM. The high-resolution TEM (HRTEM) image displays that Ag$_2$O nanoparticles are attached with ZnO nanoparticles to form ZnO/Ag$_2$O hetrostructure which improve the photocatalytic performance as shown in Fig. 5(c). In the Fig. 5(d), the interplanar distance of ZnO was found to be 0.260 nm and which match well with the (002) plane of the hexagonal wurtzite ZnO, and an inter-planar distance of 0.235 nm, assigned to the (200) plane of Ag$_2$O.
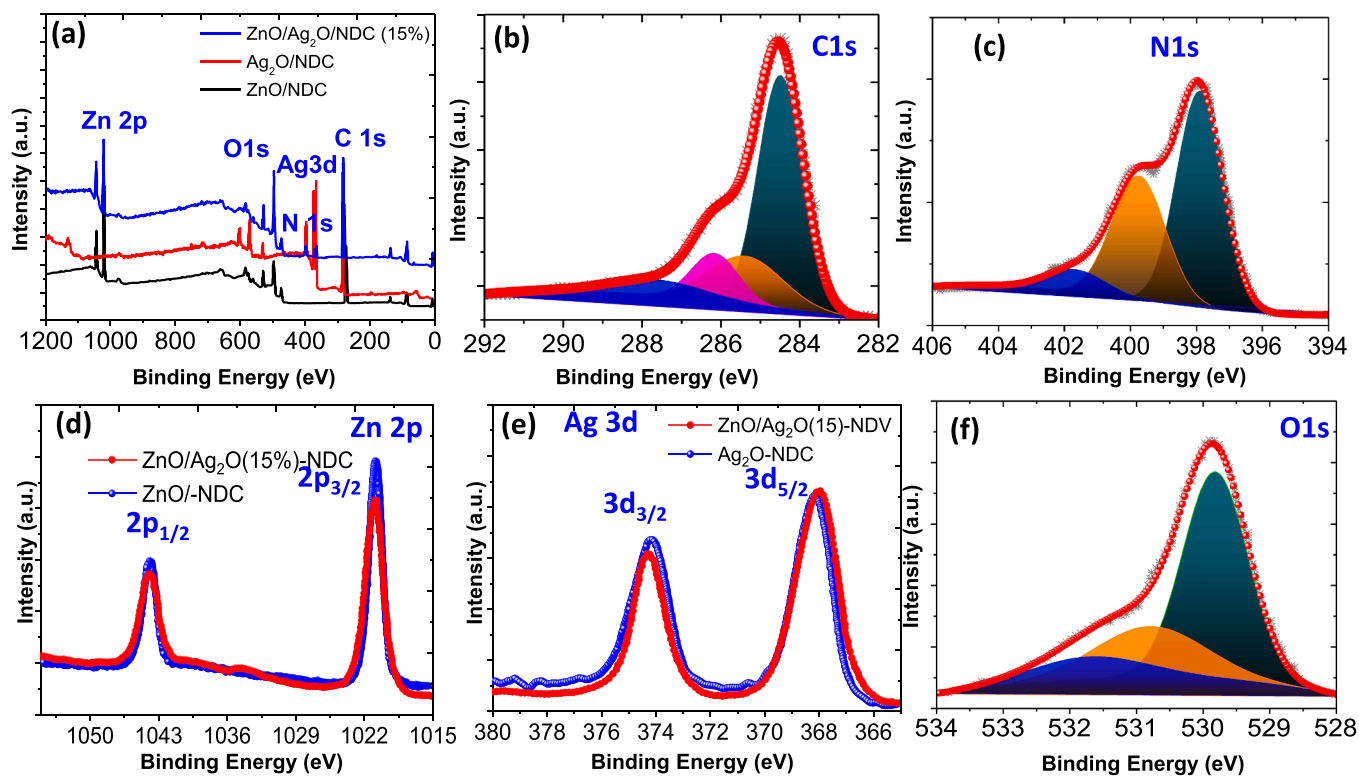
Fig. 4. (a) A wide XPS spectra for the ZnO-NDC, Ag₂O-NDC and ZnO/Ag₂O(15%)-NDC nanocomposites (b)C 1 s, (c) N 1 s (d) Zn 2p (e) Ag 3d, and (f) O 1 s of ZnO/Ag₂O(15%)-NDC.

Optical properties of the fabricated nanocomposites were determined using UV–vis diffuse reflectance absorption spectrum analysis as presented in Fig. 6(a). It was noticed that the ZnO-NDC shows strong absorption edge below to 550 nm to the ultraviolet light region below to 380 nm, owing to the inherent large band gap. On the other hand, the Ag₂O-NDC shows the adsorption in the visible region, in the range of 400–800 nm. While in the case of the hetrostructure nanocomposites, after the doping of Ag₂O, the light absorption edge of the nanocomposites ZnO/Ag₂O-NDC was changed toward the red shift [51,52]. The red shift of the absorption edge is beneficial for improving the visible light absorption capacity.

The band gap energy (E_g) was calculated by the following equation: $\alpha h\nu = A(h\nu-E_g)^{n/2}$.

where α is the absorption coefficient, A is a constant, hν is the energy of light and n is a constant depending on the nature of the electron transition.

As shown in Fig. 6(b), the band gaps of ZnO-NDC, Ag₂O-NDC, ZnO/Ag₂O(5%)-NDC, ZnO/Ag₂O(10%)-NDC, ZnO/Ag₂O(15%)-NDC and ZnO/Ag₂O(20%)-NDC were found to be 3.19, 1.49, 3.06, 3.00, 2.91 and 2.72 eV, respectively, which indicates that the band gap energy of the ZnO-NDC nanocomposite materials is reduced after the doping of Ag₂O nanoparticles, which is beneficial to improve the photocatalytic efficiency. The optical absorption features and calculated band gap values suggest that the fabricated nanocomposite materials can be used as photocatalyst under solar light. The flat band potential (E_{FB}) and band structure properties of pure ZnO-NDC and Ag₂O-NDC were confirmed using Mott-Schottky experiments. As shown in supporting figure SF-3 (a-b), the positive slope of Mott–Schottky curve of ZnO-NDC and indicating the n-type semiconductors. The E_{FB} of ZnO-NDC was found to be − 0.332 V vs an Ag/AgCl electrode, which has an E_{FB} of − 0.139 eV vs standard hydrogen electrode (NHE). On the other hand, the M-S plot of Ag₂O-NDC show the negative slope and indicating that it is a p-type semiconductor which show the E_{FB} about to 0.948 vs Ag/AgCl. Based on the results of Mott–Schottky curves, the band positions of ZnO-NDC and

Ag₂O-NDC, resulting the p–n heterojunction can be formed as displayed in supporting figure SF-3 (c).

3.2. Photocatalytic assay

The catalytic performances of the fabricated nanocomposites were carried out against the photocatalytic degradation of TC under ascribed conditions (pH 7, catalyst dose of 1.0 g/L, drug concentration of 30 mg/ L and irradiation time of 90 min). As shown in Fig. 7(a), no degradation of TC was observed in the absence of photocatalyst, indicating that self-photolysis did not occur under the irradiation of visible light, resulting in the concentration of TC being almost unchanged. While, a little concentration of TC was reduced in the dark, which could be clarified that in the absence of visible light the photocatalyst only adsorbed the TC without degradation.

Under the irradiation of visible light, about to 56.2%, 47.0%, 67.0%, 76.6%, 90.7% and 85.0% of TC degradation was noticed in the presence of ZnO-NDC, Ag₂O-NDC, ZnO/Ag₂O(5%)-NDC, ZnO/Ag₂O(10%)-NDC, ZnO/Ag₂O(15%)-NDC and ZnO/Ag₂O(20%)-NDC nanocomposites respectively. It was noticed that the coupling of Ag₂O nanoparticles with the ZnO nanoparticles increased the catalytic performance with increasing the amount of Ag₂O, but the catalytic performance was decreased when the amount of Ag₂O was increased (above 15%) this may be firstly, due to electron trapping behavior of Ag₂O and secondly, the photo-shielding effect of Ag₂O on ZnO. The degradation kinetics curves of were illustrated in Fig. 7(b), usually the photocatalytic degradation of TC follows the first-order kinetics with ln (C_0/C_t) = kt, where k is the rate constant and C_0, C_t initial and final concentration respectively [53]. It was noticed that the ZnO/Ag₂O(15%)-NDC photocatalyst show the higher value of k value, then other photocatalyst resulting, its revealed highest photocatalytic activity.

It was noticed that the initial concentration of the TC also affects the catalytic performance of the catalyst, to determine the optimum initial concentration of the TC during the photocatalytic degradation was
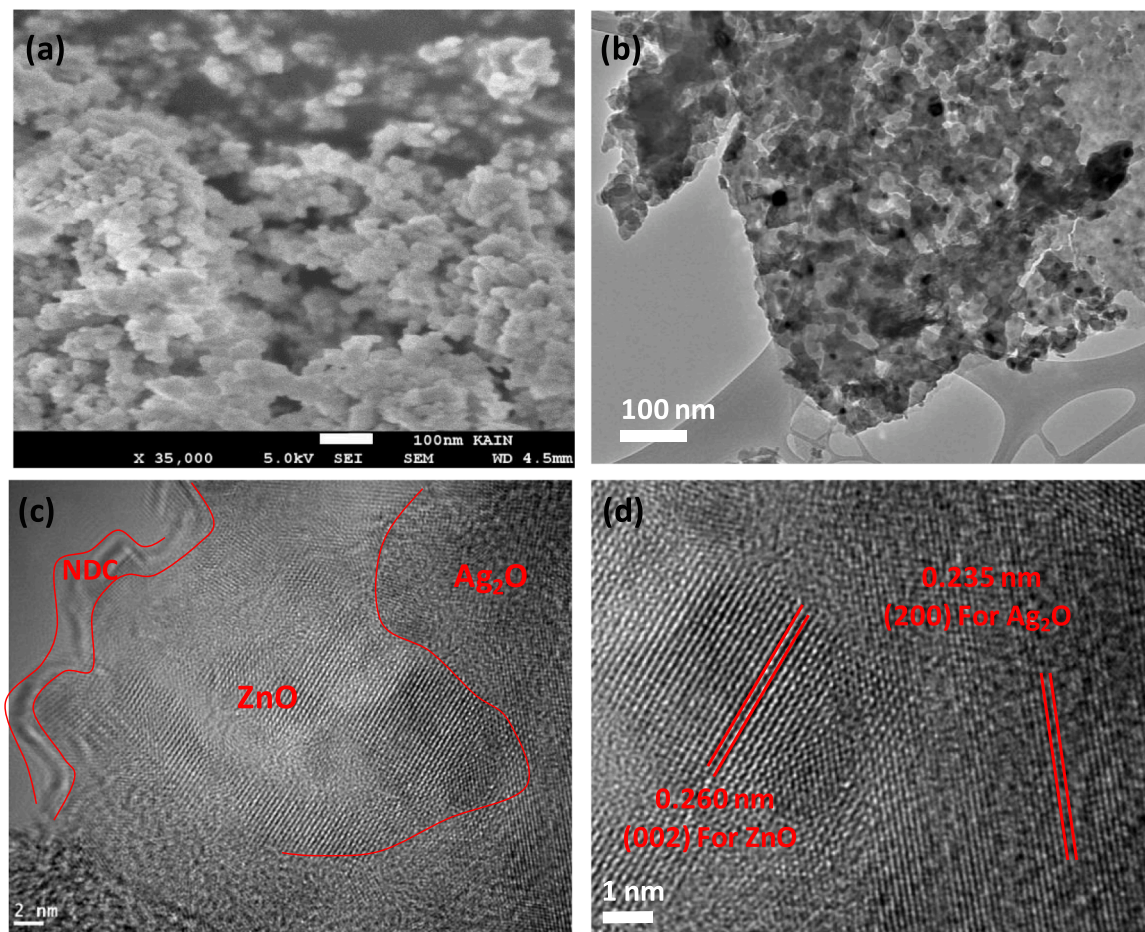
Fig. 5. (a) SEM image of ZnO/Ag₂O(15%)-NDC (b) TEM image of ZnO/Ag₂O(15%)-NDC (c) HRTEM image of ZnO/Ag₂O(15%)-NDC; and (d) HRTEM image of ZnO/Ag₂O(15%)-NDC.

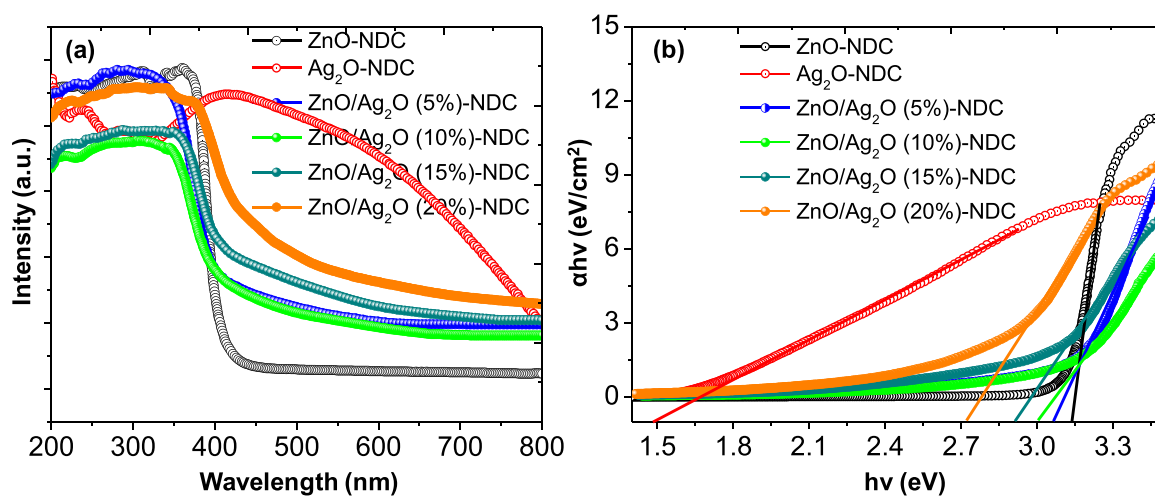**Fig. 6.** (a)UV–vis absorption spectra and (b) band gap for ZnO-NDC, Ag₂O-NDC, ZnO/Ag₂O(5%)-NDC,and ZnO/Ag₂O(15%)-NDC nanocomposites.

investigated in the range of 5 mg/L to 50 mg/L and the results are illustrated in Fig. 7(c), it was observed that the degradation performance was slightly decreased from 94.2% to 90.7% with increasing the initial concentration of TC from 5 mg/L to 30 mg/L. However, when the concentration of TC was further increased from 30 to 50 mg/L the degradation performance and the degradation rate constant was decreased and found to be 69.0% and 0.0439 min^{-1} respectively as shown in Fig. 7

(d). This may be due to the ZnO/Ag₂O(15%)-NDC active site being saturated with increasing the initial concentration, leading to the lower degradation efficiency.

To determine the optimal catalyst's dose, the experiment was carried out in the range of 0.1–2 g/L with a fixed initial concentration (30 mg/L). As shown in Fig. 8(a), It was observed that when the catalysts amount was increased form 0.1–1.0 g/L, the degradation efficiency was
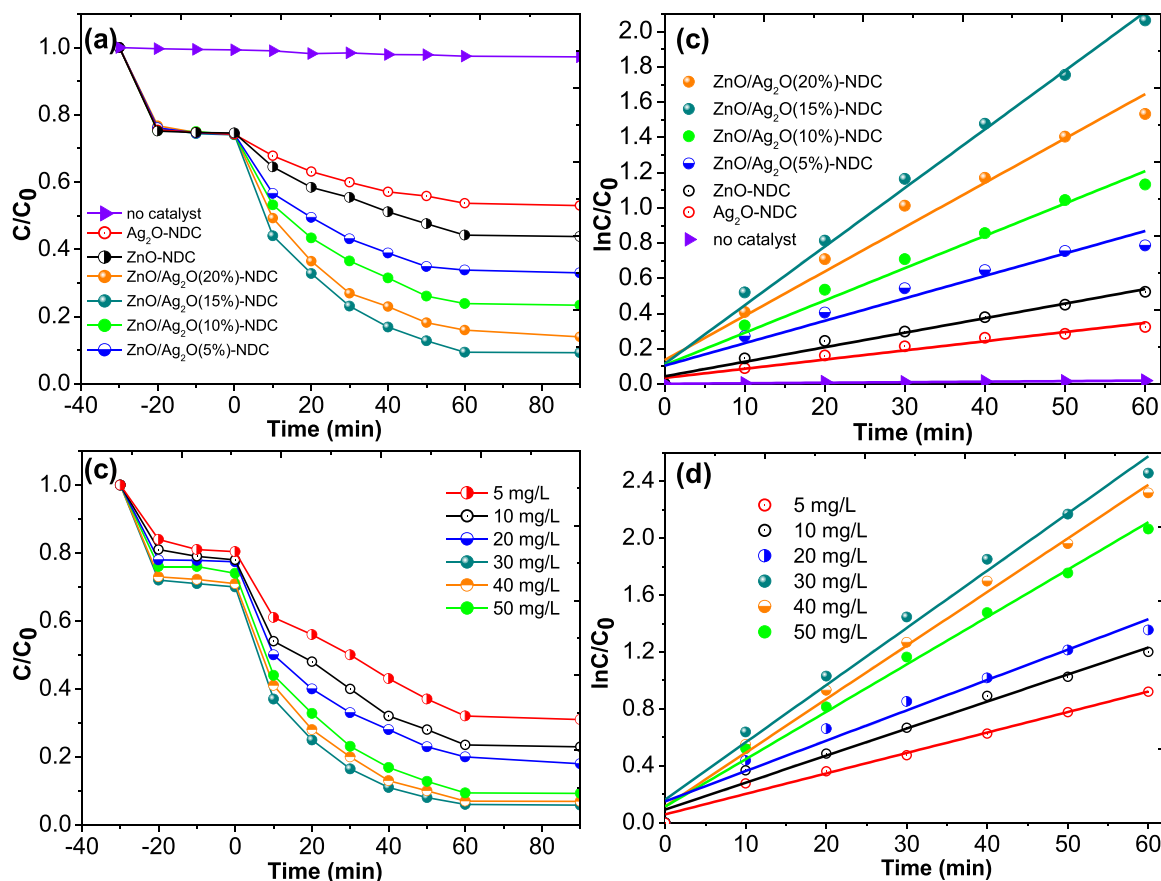
Fig. 7. (a) Photocatalytic degradation TC curves using several catalysts; (b) kinetic curves of TC degradation; (c) Effect of TC concentration during the photocatalytic degradation (d) kinetic curves of TC degradation at different concentration of TC.

increased form 48.0%– 90.7% and the rate constant was increased 0.0070–0.0333 min^{-1}, which could attribute to the increased reactive sites generating more free radicals. However, after the dose 1.0 g/L, negligible change in the degradation efficiency was observed the rate constant was decreased form 0.0333–0.0213 min^{-1} with dose 2.0 g/L, which may be due to the scattering effect and reduced the light absorption at higher dose as shown in supporting figure SF-4.

During the photocatalytic degradation of the TC, pH has a significant impact because, pH may not only affect the molecular structure of TC, but also the surface charge of catalysts and the stability of active species. As shown in figure SF-5 in supporting information, it was noticed that when the initial pH of the solution was decreased from 7 to 3 the TC degradation efficiency was decreased from 90.70 to, 52.63%, however when the pH of the solution was further increased from 7 to 10 the TC degradation efficiency was also decreased and about to 79.28% degradation was observed after 60 min. The highest degradation efficiency of TC was discovered at pH 7. The results suggested that the fabricated nanocomposite ZnO/Ag$_2$O(15%)-NDC had the best photocatalytic activity towards TC degradation under near neutral condition, while its photocatalytic activity would be inhibited under strong acid or base condition.

It was noticed that the contaminated water contains several inorganic co-existing ions including NO_3^-, Cl^-, SO_4^{2-}, and HCO_3^-, these co-existing ions, affect the photocatalytic performances of the fabricated catalysts. As illustrated in supporting figures SF-6, it was observed that no noticeable change was found on the photocatalytic degradation of TC in the presence of NO_3^- and SO_4^{2-} ions [54]. However, the presence of the Cl^- ion in the aqueous solution slightly decreased the catalytic efficiency of the ZnO/Ag$_2$O(15%)-NDC, this may be due to decreasing the adsorption of light and adulteration of the catalyst. However, the

presence of HCO_3^- ions affects the degradation of TC significantly and decreases the degradation efficiency and is found to be 62.0% of ZnO/Ag$_2$O(15%)-NDC. This may be because the HCO_3^- could react with •OH and behave as hydroxyl trapping agent. The total organic carbon (TOC) of TC was measured for the mineralization experiment and the results were shown in figure SF-7. It was observed that after 60 min, the TOC removal was found to be 63.21% while the TC degradation was noticed about to 90.70. These findings indicated that the TC molecules were first decomposed into tiny molecules (intermediates) that were more stable, followed by CO_2 and H_2O. However, the TOC curve confirms the degradation curves, and the results show that the as-fabricated photocatalyst can be employed to successfully degrade TC.

3.3. Detection of photogenerated species

The scavengers radical trapping experiments were employed to determine the types of photogenerated species during the degradation of TC degradation. For this study, ammonium oxalate (AO), 1, 4-benzoquinone (BQ), isopropyl alcohol (IPA) and silver nitrate (AgNO$_3$) were used as the scavengers for holes (h$^+$), superoxide anion radicals (•O_2^-), hydroxyl radicals (•OH) and electrons (e$^-$) respectively [55,56]. As shown in Fig. 8(b), it was observed that the degradation efficiency was decreased after the addition of all scavengers. In the presence of the AO and AgNO$_3$, slight change in the degradation efficiency was found, which may be due to the slight role of h$^+$ and e$^-$ during the TC degradation. While in the presence of BQ and IPA, decreased in the degradation efficiency was noticed, which indicates that OH• and •O_2^- has played a key role in the photocatalytic degradation of the TC in aqueous solution.

The radical-trapping results were further confirmed via EPR spectra
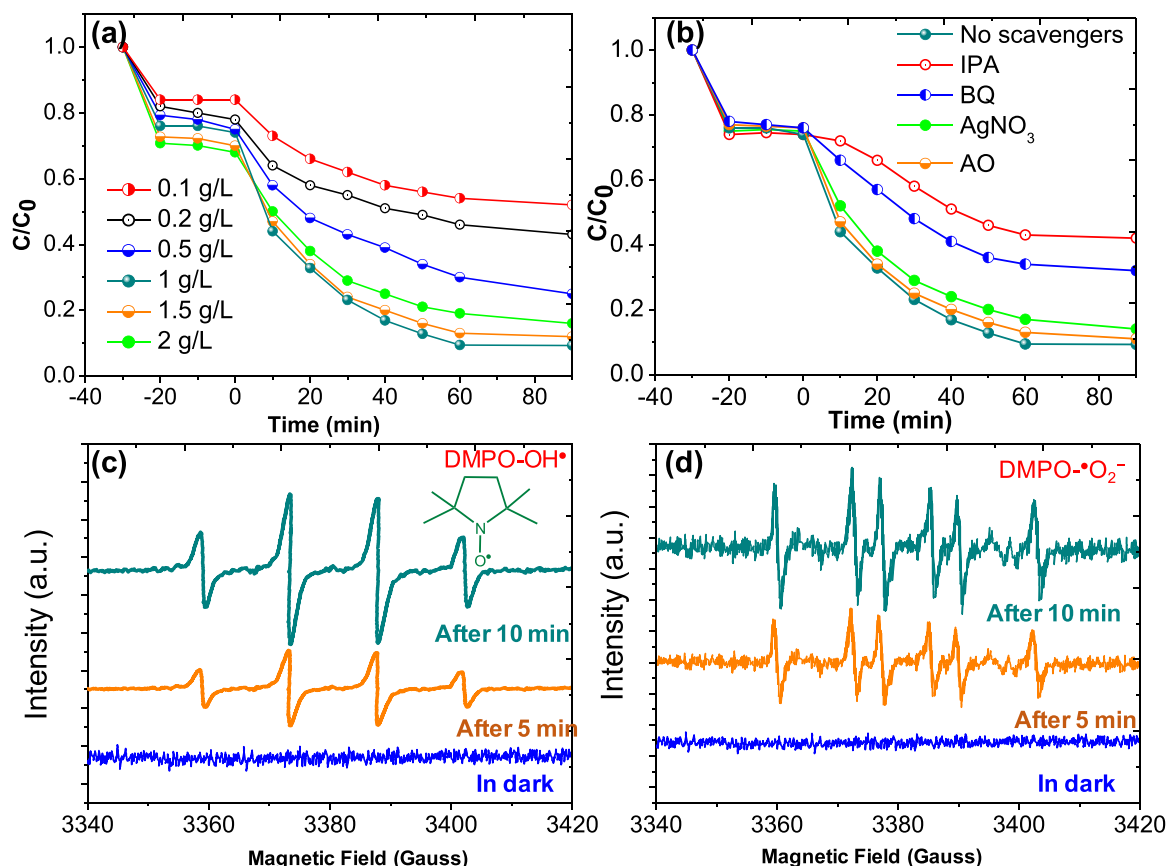
Fig. 8. (a) Effect of catalyst dose for TC degradation; (b) Effect of scavenger (d) ESR spectra of DMPO-•OH in dark and light (e) ESR spectra of DMPO-•O$_2^-$ in dark and light.

which was carried out using 5,5-dimethyl-1-pyrroline N-oxide (DMPO) technique under the dark and visible light irradiation. As shown in Fig. 8 (c and d), no EPR signal was detected in dark condition, while in both the case (DMPO-•O$_2^-$ and DMPO-•OH) four EPR signals were observed within 5 min visible irradiation, moreover the intensity of the signals was increased with increasing the visible irradiation time 10 min. The EPR analysis verified the generation and contribution of •O$_2^-$ and •OH as active radicals in the TC photodegradation.

The electrical conductivity and charge separation/recombination of photogenerated electrons-holes were investigated using photo-luminescence analysis (PL), photocurrent generation performance, and electrochemical impedance spectra (EIS). When compared to pure Ag$_2$O-NDC and ZnO-NDC, the intensity of PL spectra was decreased in the heterostructure as illustrated in figure SF-8(a). it was noticed that the PL intensity was reduced by raising the Ag$_2$O content of the nanocomposite upto 15%, while further increasing the Ag$_2$O contact increased the PL intensity. As a result, the lowest PL emission intensity of ZnO/Ag$_2$O (15%)-NDC may support the photocatalyst's effective conductive performance, thereby preventing electron-hole recombination. Figure SF-8 (b) shows the results of the photocurrent-time measurements, which show an improvement in charge transfer separation. The photocurrent was found to be higher in the ZnO/Ag$_2$O(15%)-NDC than in pure Ag$_2$O-NDC and ZnO-NDC, indicating that the mobility and separation efficiency of photoinduced charge carriers were improved with heterostructure and increased with increasing the amount of Ag$_2$O in the nanocomposite up to 15%. ESI spectra were also used to assess the photocatalyst's electrical conductivity, as illustrated in Figure SF-8 (c). On the EIS Nyquist plot, the narrow arc radius corresponds to a reduced charge transfer resistance and a higher charge transfer efficiency. The arc radius of the ZnO/Ag$_2$O(15%)-NDC nanocomposite is less than that of pure ZnO-NDC and other heterostructures (ZnO/Ag$_2$O(5%)-NDC,

ZnO/Ag$_2$O(10%)-NDC, and ZnO/Ag$_2$O(20%)-NDC), showing a lower interfacial charge-transfer resistance in the ZnO/Ag The reduction in interfacial charge-transfer resistance reveals the successful separation of electron-hole pairs, which aids photocatalytic activity.

3.3.1. Reusability of the photocatalysts

The recyclability and stability of a photocatalyst are one of the most important factors. As shown in Fig. 9(a), five consecutive cycles were tested and the results reveal that only 4% degradation efficiency was decreased after five cycles. Supporting Table (ST-1), presents the comparison of various photocatalysts from the aspects of photocatalyst dosage (g/L), pollutant concentration (mg/L), reaction time (min), and removal efficiency (%). Based on comprehensive comparison and analysis, it can be concluded that the catalyst in this work (ZnO/Ag$_2$O(15%)-NDC) exhibited an outstanding photocatalytic behavior and stability for the removal and mineralization of TC. The catalytic efficiency of the nanocomposites was decreased due to the extra trapping of electrons and conversion of Ag$^+$ into Ag as shown in Fig. 9(b). The formation of Ag metal was supported using XPS and XRD spectra. The XPS spectra of the photocatalyst after 7 cycles show the formation of Ag due to the formation of new peaks at 374.3 eV and 368.3 eV assigned to the Ag 3d$_{3/2}$ and Ag 3d$_{5/2}$ states respectively, and the slitting of the 3d doublet of Ag was 6.0 eV, indicating that the silver species existed as Ag^0.

3.4. Degradation mechanism and intermediate determination

The ionization energy and band gap of the ZnO to Ag$_2$O support the mechanism for the formation of photogenerated spices under visible light. In the ZnO/Ag$_2$O(15%)-NDC nanocomposite formed a p–n heterojunction and electron transfer occurs from ZnO to Ag$_2$O due to the ionization potential of Ag$_2$O (5.3 eV) and electron affinity of wurtzite
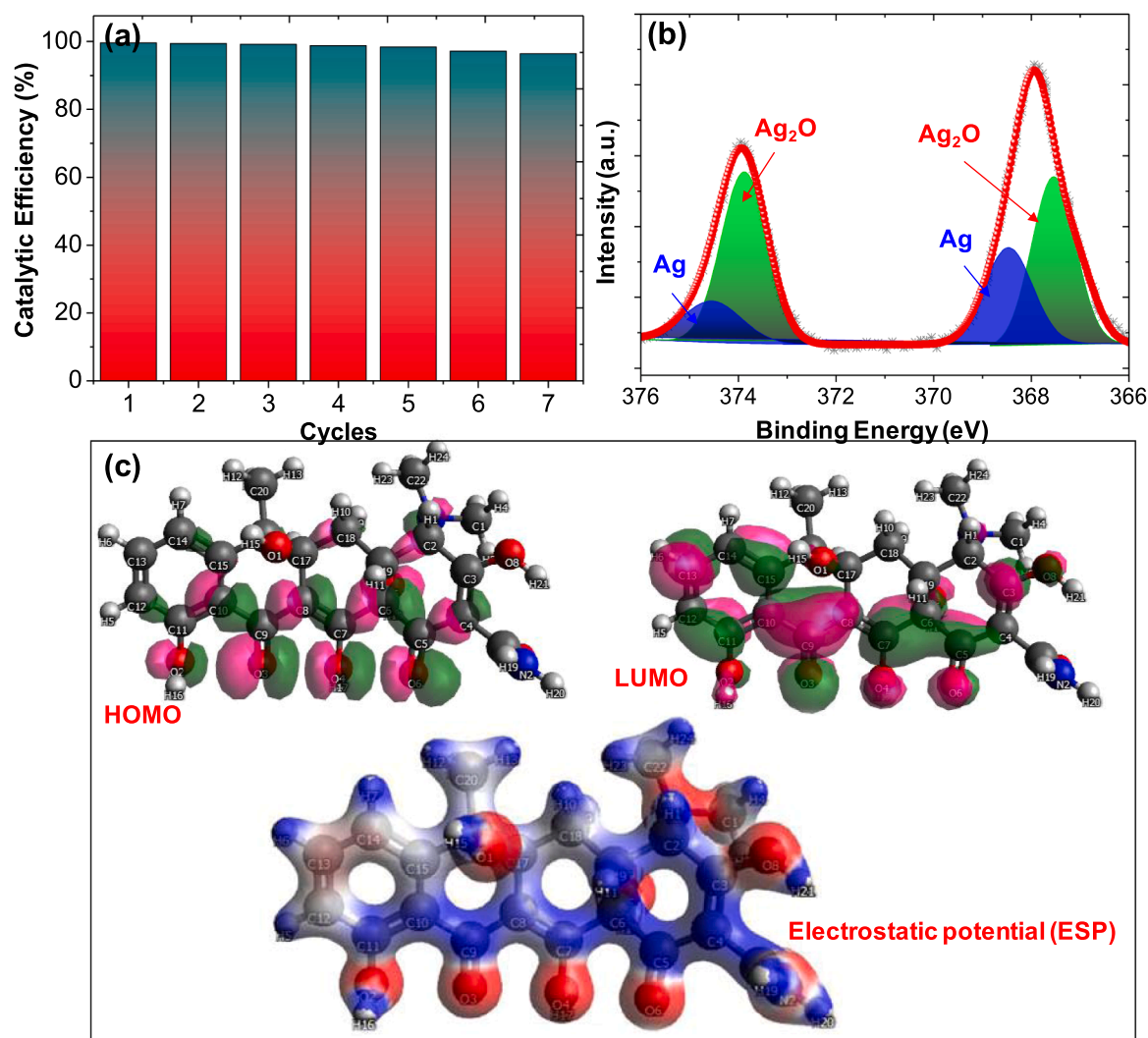
Fig. 9. (a): Reusability of the catalyst ZnO/Ag₂O(15%)-NDC (b) XPS of Ag 3d after 7 cycles (b) HOMO-LUMO and ESP of TC.
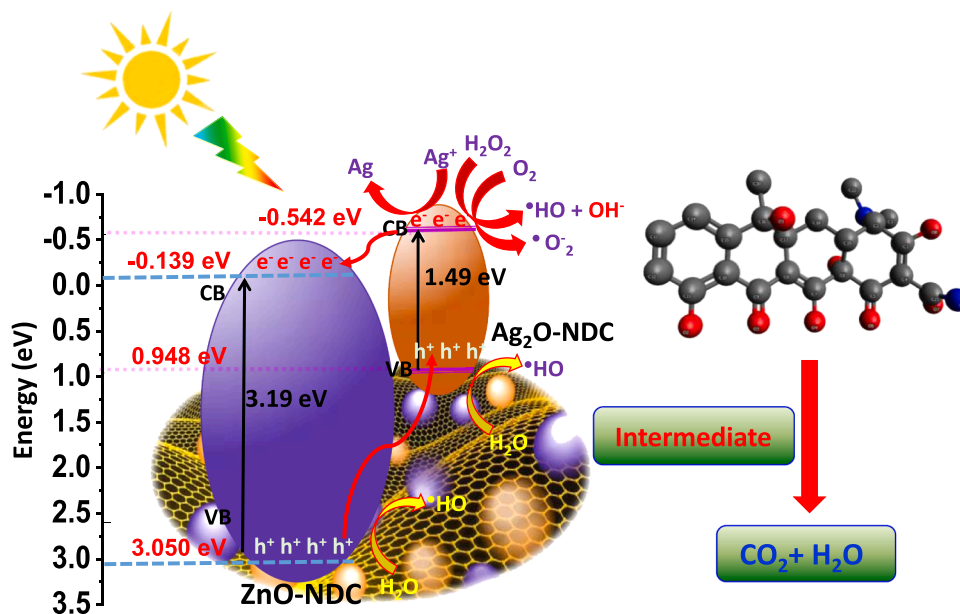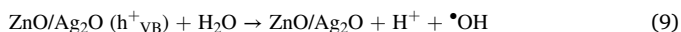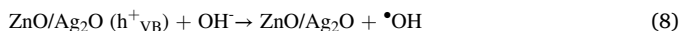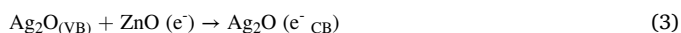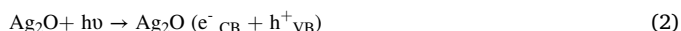

Fig. 10. Photocatalytic mechanism of ZnO/Ag₂O(15%)-NDC.

ZnO (4.3 eV). The formation of photo-induced spices was illustrated in Fig. 10 and summarized in Eqs. (1)–(10). The appropriate light source is exciting electrons at valence band (VB) edge to the conduction band (CB) and created electron-hole pairs [57–59]. Upon the photocatalytic activities under UV-light irradiation, ZnO tends to absorb more photon energy rather than Ag_2O. The photogenerated electrons from CB of ZnO site are moved in CB of Ag_2O and the photogenerated holes migrated to the VB of Ag_2O. Therefore, the prolonged charge separation could be effectively improved by p-n heterojunction and lead to the enhancement of photocatalytic activities. While the holes (h^+) were remains into the VB of both ZnO to Ag_2O, generate HO_2^- and further generate $^•OH$, $^•HO_2$ and H_2O_2. While the formed e^- were further transfer to the CB of Ag_2O, and react with the available O_2 to produced $^•O_2^-$.

Additionally, the electrons can be trapped with the silver ions which could effectively inhibit the recombination of the photoinduced electron-hole pairs.

$$ZnO + h\upsilon \rightarrow ZnO(\ h^+_{VB} + e^-) \tag{1}$$

$$Ag_2O + h\upsilon \rightarrow Ag_2O\ (e^-_{\ CB} + h^+_{\ VB}) \tag{2}$$

$$Ag_2O_{(VB)} + ZnO\ (e^-) \rightarrow Ag_2O\ (e^-_{\ CB}) \tag{3}$$

$$Ag_2O(e^-_{\ CB}) + O_2 \rightarrow Ag_2O + ^•O_2^- \tag{4}$$

$$^•O_2^- + H^+ \rightarrow ^•OH_2 \tag{5}$$

$$Ag_2O\ (e^-_{\ CB}) + ^•O_2^- + H^+ \rightarrow ^•OH_2^- \tag{6}$$

$$^•OH_2^- + h^+ \rightarrow H_2O_2 \tag{7}$$

$$ZnO/Ag_2O\ (h^+_{\ VB}) + OH^- \rightarrow ZnO/Ag_2O + ^•OH \tag{8}$$

$$ZnO/Ag_2O\ (h^+_{\ VB}) + H_2O \rightarrow ZnO/Ag_2O + H^+ + ^•OH \tag{9}$$

$$TC + (h+, ^•OH, ^•O_2^-, e^-) \rightarrow intermediates \rightarrow CO_2 + H_2O \tag{10}$$

The photocatalytic degradation pathway and formation of intermediates during the photocatalytic degradation of TC under visible light irradiation was explained using LC-MS analysis (as summarized in supporting table-3) and supported via chemical computation based on DFT techniques. The active sites on the TC molecule for photocatalytic degradation were predicted using Fukui function calculation and the highest occupied molecular orbital (HOMO) and lowest unoccupied molecular orbital (LUMO) of TC have been illustrated in Fig. 9(c). In addition, electrostatic potential (ESP) mapping indicate the regions of TC molecules, which could easily bind with the photogenerated species. As the Fukui index summarized in supporting table-2, the atoms marked with red color exhibit relatively larger f^0 such as C8, C4, N2 and C2, are more vulnerable to radical attack. By combining the detected intermediates and Fukui index, the photo-degradation pathway of TC is presented in Fig. 11. The TC degradation can be explained in two pathways, in the first degradation pathway, the hydroxylation reaction was carried out at C8 due to most reactive site ($f^+ = 0.0915$, $f^° = 0.0845$), and to be attacked by $^•OH$ radicals, resulting the formation of hydroxylated TC intermediate **B** (m/z 461), which was further supported via GC-MS spectra. Subsequently, the intermediate B was further attacked by $^•OH$ radicals and produced intermediate **C** with m/z 477. After 30 min, in the GC-MS spectra the peak belong to TC at $m/z = 445$ was completely disappear and another peaks were found at $m/z = 231$, 140, and 125 due to the formation of new intermediate by breaking the methyl, amino and hydroxyl groups. Moreover, the attacked by $^•OH$ to produce smaller intermediates and then volatile compounds after cleaving the aromatic rings. The second pathway is observed due to the removal of –NH group form the N2 atom ($f^+ = 0.0248$, $f^° = 0.2321$) which was attacked by the $^•O_2^-$ and resulting in formation of intermediate **D** with m/z 430**(C)**. The intermediate **D** was further degraded after the cleavage of –CO from the C4 and generated another intermediate E with m/z 402. As the retention time was increased the small molecular weight intermediates are obtained after the bond and ring cleavage using OH and $^•O_2^-$ and show several GC-MS peaks belongs to smaller intermediates. It was noticed that after 60 min TC molecules were completely degraded with photogenerated free radicals into volatile compounds such as to CO_2, H_2O, and inorganic ions NH_4^+, NH_3.
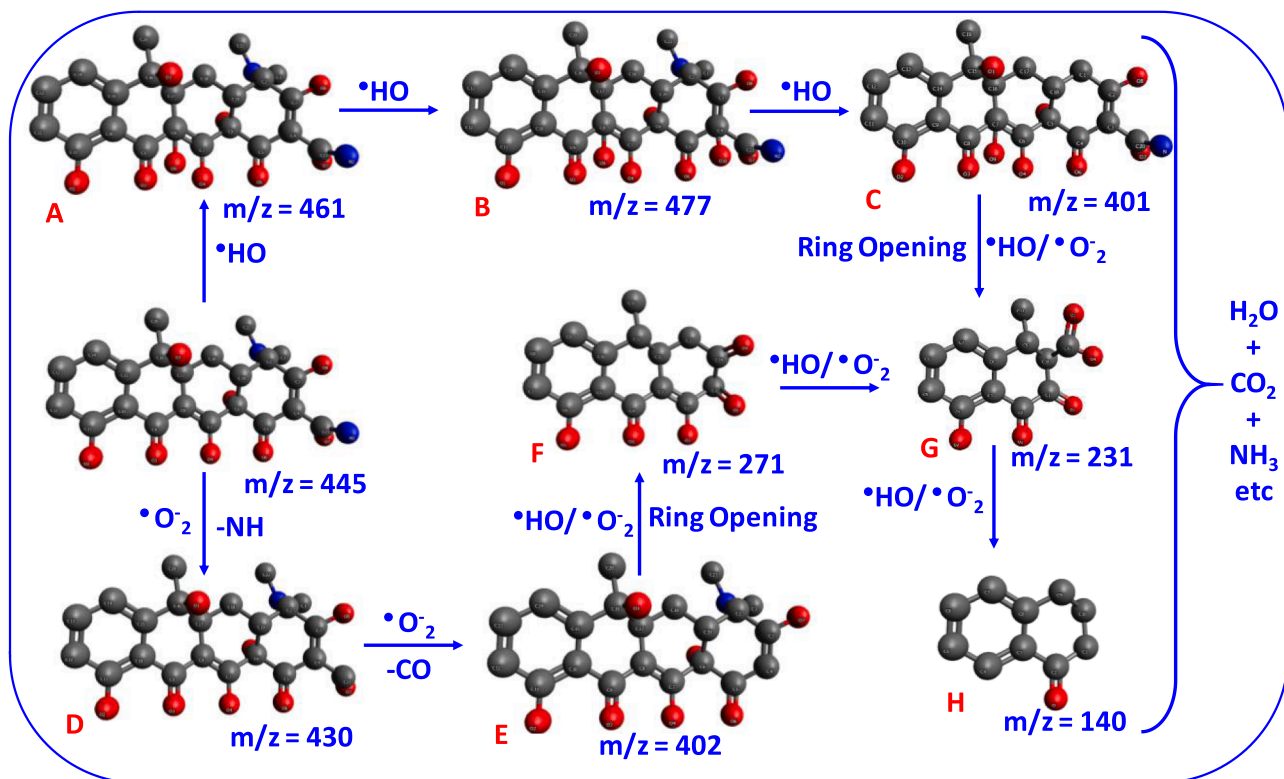

Fig. 11. Photocatalytic degradation pathways for the TC.

4. Conclusion

In summary, the novel photocatalyst hetrostructure was fabricated using egg albumin. The chemical composition, structure and the morphology, surface area of the prepared nanocomposites was determined using analytical techniques. The fabricated ZnO/Ag$_2$O(15%)-NDC show excellent photodegradation of TC at room temperature under visible light. The results revealed that about 90.7% TC was decomposed within 60 min at optimum condition and followed the first order reaction with a rate constant of 0.0333 min^{-1}. The ESR and trapping results support the formation of photogenerated spices OH$^{\bullet}$ and $^{\bullet}$O$_2$$^{-}$, which plays the main role during the TC degradation. The mechanism was demonstrated combining the theoretical calculation with experimental data. Over all, the fabrication of the nanocomposites using egg albumen is facile, effective, cost efficient, fast and suitable and can be used for the fabrication of other photocatalysts and can be used for water treatment, environmental cleaning on industrial scale.

Declaration of Competing Interest

The authors declare that they have no known competing financial interests or personal relationships that could have appeared to influence the work reported in this paper.

Acknowledgement

Appendix A. Supporting information

Supplementary data associated with this article can be found in the online version at doi:10.1016/j.jece.2022.107681.

References

[1] S. Hussain, M. Mottahir Alam, M. Imran, M. Ashraf Ali, T. Ahamad, A.S. Haidyrah, S.M.A. Raji Alotaibi, M.-u-d Naik, M. Shariq, A facile low-cost scheme for highly photoactive Fe3O4-MWCNTs nanocomposite material for degradation of methylene blue, Alex. Eng. J. 61 (11) (2022) 9107–9117.

[2] K. Perumal, S. Shanavas, T. Ahamad, A. Karthigeyan, P. Murugakoothan, Construction of Ag2CO3/BiOBr/CdS ternary composite photocatalyst with improved visible-light photocatalytic activity on tetracycline molecule degradation, J. Environ. Sci. 125 (2023) 47–60.

[3] S. Shanavas, M.A. Haija, D.P. Singh, T. Ahamad, S.M. Roopan, Q. Van Le, R. Acevedo, P.M. Anbarasan, Development of high efficient Co3O4/Bi2O3/rGO nanocomposite for an effective photocatalytic degradation of pharmaceutical molecules with improved interfacial charge transfer, J. Environ. Chem. Eng. 10 (2) (2022), 107243.

[4] S. Sharma, V. Dutta, P. Raizada, V. Kumar Thakur, A.K. Saini, D. Mittal, V.-H. Nguyen, T. Ahamad, C. Chien Nguyen, S. Young Kim, Q.V. Le, P. Singh, Synergistic photocatalytic dye mitigation and bacterial disinfection using carbon quantum dots decorated dual Z-scheme Manganese Indium Sulfide/Cuprous Oxide/Silver oxide heterojunction, Mater. Lett. 313 (2022) 131716.

[5] T. Tang, Z. Yin, J. Chen, S. Zhang, W. Sheng, W. Wei, Y. Xiao, Q. Shi, S. Cao, Novel p-n heterojunction Bi2O3/Ti3+-TiO2 photocatalyst enables the complete removal of tetracyclines under visible light, Chem. Eng. J. (2020), 128058.

[6] S. Yan, J. Yang, Y. Li, X. Jia, H. Song, One-step synthesis of ZnS/BiOBr photocatalyst to enhance photodegradation of tetracycline under full spectral irradiation, Mater. Lett. 276 (2020), 128232.

[7] Q. Zhang, L. Jiang, J. Wang, Y. Zhu, Y. Pu, W. Dai, Photocatalytic degradation of tetracycline antibiotics using three-dimensional network structure perylene diimide supramolecular organic photocatalyst under visible-light irradiation, Appl. Catal. B: Environ. 277 (2020), 119122.

[8] T. Ahamad, M. Naushad, S.I. Al-Saeedi, S. Almotairi, S.M. Alshehri, Fabrication of MoS2/ZnS embedded in N/S doped carbon for the photocatalytic degradation of pesticide, Mater. Lett. 263 (2020), 127271.

[9] T. Ahamad, M. Naushad, S.I. Al-Saeedi, S.M. Alshehri, N/S-doped carbon embedded with AgNPs as a highly efficient catalyst for the reduction of toxic organic pollutants, Mater. Lett. 264 (2020), 127310.

[10] T. Ahamad, M. Naushad, S.M. Alshehri, Analysis of degradation pathways and intermediates products for ciprofloxacin using a highly porous photocatalyst, Chem. Eng. J. (2020), 127969.

[11] T. Ahamad, M. Naushad, Y. Alzaharani, S.M. Alshehri, Photocatalytic degradation of bisphenol-A with g-C3N4/MoS2-PANI nanocomposite: Kinetics, main active species, intermediates and pathways, J. Mol. Liq. 311 (2020), 113339.

[12] N.S. Alhokbany, R. Mousa, M. Naushad, S.M. Alshehri, T. Ahamad, Fabrication of Z-scheme photocatalysts g-C3N4/Ag3PO4/chitosan for the photocatalytic degradation of ciprofloxacin, Int. J. Biol. Macromol. 164 (2020) 3864–3872.

[13] A.A. Al-Kahtani, S.M. Alshehri, M. Naushad, Ruksana, T. Ahamad, Fabrication of highly porous N/S doped carbon embedded with ZnS as highly efficient photocatalyst for degradation of bisphenol, Int. J. Biol. Macromol. 121 (2019) 415–423.

[14] S.S. Chen, C. Hu, C.-H. Liu, Y.-H. Chen, T. Ahamad, S.M. Alshehri, P.-H. Huang, K. C.W. Wu, De Novo synthesis of platinum-nanoparticle-encapsulated UiO-66-NH2 for photocatalytic thin film fabrication with enhanced performance of phenol degradation, J. Hazard. Mater. 397 (2020), 122431.

[15] A. Kumar, G. Sharma, M. Naushad, T. Ahamad, R.C. Veses, F.J. Stadler, Highly visible active Ag2CrO4/Ag/BiFeO3@RGO nano-junction for photoreduction of CO2 and photocatalytic removal of ciprofloxacin and bromate ions: The triggering effect of Ag and RGO, Chem. Eng. J. 370 (2019) 148–165.

[16] A. Kumar, G. Sharma, M. Naushad, A. a H. Al-Muhtaseb, A. Kumar, I. Hira, T. Ahamad, A.A. Ghfar, F.J. Stadler, Visible photodegradation of ibuprofen and 2,4-D in simulated waste water using sustainable metal free-hybrids based on carbon nitride and biochar, J. Environ. Manag. 231 (2019) 1164–1175.

[17] D. Pathania, D. Gupta, A. a H. Al-Muhtaseb, G. Sharma, A. Kumar, M. Naushad, T. Ahamad, S.M. Alshehri, Photocatalytic degradation of highly toxic dyes using chitosan-g-poly(acrylamide)/ZnS in presence of solar irradiation, J. Photochem. Photobiol. A: Chem. 329 (2016) 61–68.

[18] G. Sharma, A. Kumar, M. Naushad, A. García-Peñas, A. a H. Al-Muhtaseb, A. A. Ghfar, V. Sharma, T. Ahamad, F.J. Stadler, Fabrication and characterization of Gum arabic-cl-poly(acrylamide) nanohydrogel for effective adsorption of crystal violet dye, Carbohydr. Polym. 202 (2018) 444–453.

[19] K. Bhuvaneswari, G. Palanisamy, K. Sivashanmugan, T. Pazhanivel, T. Maiyalagan, ZnO nanoparticles decorated multiwall carbon nanotube assisted ZnMgAl layered triple hydroxide hybrid photocatalyst for visible light-driven organic pollutants removal, J. Environ. Chem. Eng. 9 (1) (2021), 104909.

[20] C.-J. Chang, J.-K. Chen, K.-S. Lin, C.-Y. Huang, C.-L. Huang, Improved H2 production of ZnO@ZnS nanorod-decorated Ni foam immobilized photocatalysts, Int. J. Hydrog. Energy (2020).

[21] K.H. Ng, K. Chen, C.K. Cheng, D.-V.N. Vo, Elimination of energy-consuming mechanical stirring: development of auto-suspending ZnO-based photocatalyst for organic wastewater treatment, J. Hazard. Mater. (2020), 124532.

[22] S. Deebansok, T. Amornsakchai, P. Sae-ear, P. Siriphannon, S.M. Smith, Sphere-like and flake-like ZnO immobilized on pineapple leaf fibers as easy-to-recover photocatalyst for the degradation of congo red, J. Environ. Chem. Eng. (2020), 104746.

[23] M.H. Elsayed, T.M. Elmorsi, A.M. Abuelela, A.E. Hassan, A.Z. Alhakemy, M.F. Bakr, H.-H. Chou, Direct sunlight-active Na-doped ZnO photocatalyst for the mineralization of organic pollutants at different pH mediums, J. Taiwan Inst. Chem. Eng. 115 (2020) 187–197.

[24] R. Gang, L. Xu, Y. Xia, J. Cai, L. Zhang, S. Wang, R. Li, Fabrication of MoS2 QDs/ ZnO nanosheet 0D/2D heterojunction photocatalysts for organic dyes and gaseous heavy metal removal, J. Colloid Interface Sci. 579 (2020) 853–861.

[25] N. Raza, W. Raza, H. Gul, K.-H. Kim, ZnO–ZnTe hierarchical superstructures as solar-light-activated photocatalysts for azo dye removal, Environ. Res. (2020), 110499.

[26] T. Senasu, T. Chankhanittha, K. Hemavibool, S. Nanan, Visible-light-responsive photocatalyst based on ZnO/CdS nanocomposite for photodegradation of reactive red azo dye and ofloxacin antibiotic, Mater. Sci. Semicond. Process. 123 (2021), 105558.

[27] D. Tekin, H. Kiziltas, H. Ungan, Kinetic evaluation of ZnO/TiO2 thin film photocatalyst in photocatalytic degradation of Orange G, J. Mol. Liq. 306 (2020), 112905.

[28] M.A. Qamar, S. Shahid, M. Javed, S. Iqbal, A. Bahadur, D. Li, Fabricated novel g-C3N4/Mn doped ZnO nanocomposite as highly active photocatalyst for the disinfection of pathogens and degradation of the organic pollutants from wastewater under sunlight radiations, Colloids Surf. A: Physicochem. Eng. Asp. 611 (2021), 125863.

[29] K. Sabzehei, S.H. Hadavi, M.G. Bajestani, S. Sheibani, Comparative evaluation of copper oxide nano-photocatalyst characteristics by formation of composite with TiO2 and ZnO, Solid State Sci. 107 (2020), 106362.

[30] V. Sharma, V. Maivizhikannan, V.N. Rao, S. Kumar, A. Kumar, A. Kumar, M. V. Shankar, V. Krishnan, Sea urchin shaped ZnO coupled with MoS2 and polyaniline as highly efficient photocatalysts for organic pollutant decomposition and hydrogen evolution, Ceram. Int. (2020).

[31] K. Kalpana, V. Selvaraj, A novel approach for the synthesis of highly active ZnO/ TiO2/Ag2O nanocomposite and its photocatalytic applications, Ceram. Int. 41 (8) (2015) 9671–9679.

[32] Y. Liu, P. Li, R. Xue, X. Fan, Research on catalytic performance and mechanism of Ag2O/ZnO heterostructure under UV and visible light, Chem. Phys. Lett. 746 (2020), 137301.

[33] X. Rong, F. Qiu, Z. Jiang, J. Rong, J. Pan, T. Zhang, D. Yang, Preparation of ternary combined ZnO-Ag2O/porous g-C3N4 composite photocatalyst and enhanced visible-light photocatalytic activity for degradation of ciprofloxacin, Chem. Eng. Res. Des. 111 (2016) 253–261.

[34] M. Ahmad, S.J.A. Zaidi, S. Zoha, M.S. Khan, M. Shahid, T.J. Park, M.A. Basit, Pseudo-SILAR assisted unique synthesis of ZnO/Ag2O nanocomposites for

improved photocatalytic and antibacterial performance without cytotoxic effect, Colloids Surf. A: Physicochem. Eng. Asp. 603 (2020), 125200.

[35] M. Anjum, R. Kumar, H.A. Al-Talhi, S.A. Mohamed, M.A. Barakat, Valorization of biogas production through disintegration of waste activated sludge using visible light ZnO-ZnS/Ag2O-Ag2S photocatalyst, Process Saf. Environ. Prot. 119 (2018) 330–339.

[36] W. Ding, L. Zhao, H. Yan, X. Wang, X. Liu, X. Zhang, X. Huang, R. Hang, Y. Wang, X. Yao, B. Tang, Bovine serum albumin assisted synthesis of Ag/Ag2O/ZnO photocatalyst with enhanced photocatalytic activity under visible light, Colloids Surf. A: Physicochem. Eng. Asp. 568 (2019) 131–140.

[37] A. Velumani, P. Sengodan, P. Arumugam, R. Rajendran, S. Santhanam, M. Palanisamy, Carbon quantum dots supported ZnO sphere based photocatalyst for dye degradation application, Curr. Appl. Phys. 20 (10) (2020) 1176–1184.

[38] S. Zarezadeh, A. Habibi-Yangjeh, M. Mousavi, S. Ghosh, Novel ZnO/Ag3PO4/AgI photocatalysts: Preparation, characterization, and the excellent visible-light photocatalytic performances, Mater. Sci. Semicond. Process. 119 (2020), 105229.

[39] P. Zhu, M. Hu, M. Duan, L. Xie, M. Zhao, High visible light response Z-scheme Ag3PO4 / g-C3N4 / ZnO composite photocatalyst for efficient degradation of tetracycline hydrochloride: Preparation, properties and mechanism, J. Alloy. Compd. 840 (2020), 155714.

[40] L. Huang, D. Bao, X. Jiang, J. Li, L. Zhang, X. Sun, Fabrication of stable high-performance urchin-like CeO2/ZnO@Au hierarchical heterojunction photocatalyst for water remediation, J. Colloid Interface Sci. (2020).

[41] K. Karuppasamy, I. Rabani, D. Vikraman, C. Bathula, J. Theerthagiri, R. Bose, C.-J. Yim, A. Kathalingam, Y.-S. Seo, H.-S. Kim, ZIF-8 templated assembly of La3+-anchored ZnO distorted nano-hexagons as an efficient active photocatalyst for the detoxification of rhodamine B in water, Environ. Pollut. (2020) 116018.

[42] R.M. Mohamed, A.A. Ismail, Photocatalytic reduction and removal of mercury ions over mesoporous CuO/ZnO S-scheme heterojunction photocatalyst, Ceram. Int. (2020).

[43] N. Rosman, W.N.W. Salleh, M.A. Mohamed, Z. Harun, A.F. Ismail, F. Aziz, Constructing a compact heterojunction structure of Ag2CO3/Ag2O in-situ intermediate phase transformation decorated on ZnO with superior photocatalytic degradation of ibuprofen, Sep. Purif. Technol. 251 (2020), 117391.

[44] H. Salari, M. Sadeghinia, MOF-templated synthesis of nano Ag2O/ZnO/CuO heterostructure for photocatalysis, J. Photochem. Photobiol. A: Chem. 376 (2019) 279–287.

[45] S.M. Alshehri, A.N. Alhabarah, J. Ahmed, M. Naushad, T. Ahamad, An efficient and cost-effective tri-functional electrocatalyst based on cobalt ferrite embedded nitrogen doped carbon, J. Colloid Interface Sci. 514 (2018) 1–9.

[46] H. Tan, J. Kim, J. Lin, C. Li, S.M. Alsheri, T. Ahamad, N. Alhokbany, Y. Bando, M. Zaman, M.S.A. Hossain, A facile surfactant-assisted synthesis of carbon-supported dendritic Pt nanoparticles with high electrocatalytic performance for the oxygen reduction reaction, Microporous Mesoporous Mater. 280 (2019) 1–6.

[47] J.-C. Shen, H.-Y. Zeng, C.-R. Chen, S. Xu, A facile fabrication of Ag2O-Ag/ZnAl-oxides with enhanced visible-light photocatalytic performance for tetracycline degradation, Appl. Clay Sci. 185 (2020), 105413.

[48] E. Torad, E.H. Ismail, M.M. Mohamed, M.M.H. Khalil, Tuning the redox potential of Ag@Ag2O/WO3 and Ag@Ag2S/WO3 photocatalysts toward diclofenac oxidation and nitrophenol reduction, Mater. Res. Bull. 137 (2021), 111193.

[49] Y. Ma, Y. Guo, H. Jiang, D. Qu, J. Liu, W. Kang, Y. Yi, W. Zhang, J. Shi, Z. Han, Preparation of network-like ZnO–FeWO4 mesoporous heterojunctions with tunable band gaps and their enhanced visible light photocatalytic performance, N. J. Chem. 39 (7) (2015) 5612–5620.

[50] M. Naushad, T. Ahamad, B.M. Al-Maswari, A.A. Alqadami, S.M. Alshehri, Nickel ferrite bearing nitrogen-doped mesoporous carbon as efficient adsorbent for the removal of highly toxic metal ion from aqueous medium, Chem. Eng. J. 330 (2017) 1351–1360.

[51] P. Xu, P. Wang, Q. Wang, R. Wei, Y. Li, Y. Xin, T. Zheng, L. Hu, X. Wang, G. Zhang, Facile synthesis of Ag2O/ZnO/rGO heterojunction with enhanced photocatalytic activity under simulated solar light: Kinetics and mechanism, J. Hazard. Mater. 403 (2021), 124011.

[52] S. Zoha, M. Ahmad, S.J.A. Zaidi, M.N. Ashiq, W. Ahmad, T.J. Park, M.A. Basit, ZnO-based mutable Ag2S/Ag2O multilayered architectures for organic dye degradation and inhibition of E. coli and B. subtilis, J. Photochem. Photobiol. A: Chem. 394 (2020), 112472.

[53] Y. Deng, L. Tang, C. Feng, G. Zeng, J. Wang, Y. Zhou, Y. Liu, B. Peng, H. Feng, Construction of plasmonic Ag modified phosphorous-doped ultrathin g-C3N4 nanosheets/BiVO4 photocatalyst with enhanced visible-near-infrared response ability for ciprofloxacin degradation, J. Hazard. Mater. 344 (2018) 758–769.

[54] R. Wang, P. Zhu, M. Duan, J. Xu, M. Liu, D. Luo, Synthesis and characterization of successive Z-scheme CdS/Bi2MoO6/BiOBr heterojunction photocatalyst with efficient performance for antibiotic degradation, J. Alloy. Compd. 870 (2021), 159385.

[55] S. Wang, D. Li, C. Sun, S. Yang, Y. Guan, H. He, Synthesis and characterization of g-C3N4/Ag3VO4 composites with significantly enhanced visible-light photocatalytic activity for triphenylmethane dye degradation, Appl. Catal. B: Environ. 144 (2014) 885–892.

[56] S. Lin, W. Cui, X. Li, H. Sui, Z. Zhang, Cu2O NPs/Bi2O2CO3 flower-like complex photocatalysts with enhanced visible light photocatalytic degradation of organic pollutants, Catal. Today 297 (2017) 237–245.

[57] R. Wang, P. Zhu, M. Liu, J. Xu, M. Duan, D. Luo, Synthesis and characterization of magnetic ZnFe2O4/Bi0-Bi2MoO6 with Z-scheme heterojunction for antibiotics degradation under visible light, Sep. Purif. Technol. 277 (2021), 119339.

[58] P. Zhu, M. Duan, R. Wang, J. Xu, P. Zou, H. Jia, Facile synthesis of ZnO/GO/Ag3PO4 heterojunction photocatalyst with excellent photodegradation activity for tetracycline hydrochloride under visible light, Colloids Surf. A: Physicochem. Eng. Asp. 602 (2020), 125118.

[59] P. Zhu, Y. Chen, M. Duan, Z. Ren, M. Hu, Construction and mechanism of a highly efficient and stable Z-scheme Ag3PO4/reduced graphene oxide/Bi2MoO6 visible-light photocatalyst, Catal. Sci. Technol. 8 (15) (2018) 3818–3832.